Journal of Pain Research

Dovepress
Taylor & Francis Group

ORIGINAL RESEARCH

A Novel Mobile C-Arm Fluoroscopic Imaging of the Foramen Ovale and Its Anatomical Principles

Ting Qiu[1],*, Qiancheng Guo[1],*, Tengxiao Kong[1], Menglei Yin[1], Qian Bai[2], Mengdi Zhang[3], Genwei Wang[1], Shengzhong Tao[1], Zhan Liu[1]

[1]Department of Neurosurgery, The Second Affiliated Hospital of Zhengzhou University, Zhengzhou, Henan, People's Republic of China; [2]Department of Anesthesiology, The Second Affiliated Hospital of Zhengzhou University, Zhengzhou, Henan, People's Republic of China; [3]Department of Medical Imaging, The Second Affiliated Hospital of Zhengzhou University, Zhengzhou, Henan, People's Republic of China

*These authors contributed equally to this work

Correspondence: Zhan Liu, Department of Neurosurgery, The Second Affiliated Hospital of Zhengzhou University, Zhengzhou, Henan, People's Republic of China, Tel +86 0371 63620615, Email tomliuz2009@gmail.com

---

Purpose: Accurate localization of the foramen ovale (FO) is essential for percutaneous balloon compression, radiofrequency thermocoagulation, and glycerol injection in the treatment of trigeminal neuralgia. The mobile C-arm X-ray system is widely used due to its accessibility and low radiation exposure, but achieving optimal positioning to visualize the FO remains challenging. We propose a novel approach using facial surface landmarks to guide rapid and accurate C-arm positioning for FO fluoroscopy.

Patients and Methods: Patients were placed in the supine position, and three anatomical reference points were identified: Point A (subnasale), marked with a metal marker, and Points B and C (the intersections of the lateral orbital margins and the superior extensions of the zygomatic arches bilaterally), marked with surgical ink. With the X-ray tube of the C-arm centered above the face, the device was rotated along the transverse axis toward the foot end until Points A, B, and C appeared collinear from the tube's eye view. Fluoroscopy was then used to confirm alignment of Point A with the line connecting the outermost points of the bilateral infraorbital margins. Finally, the tube was tilted 20–25° toward the puncture side along its curved rail to visualize the FO. This method was validated through virtual simulation, intraoperative fluoroscopy, and 3D anatomical modeling.

Results: Clear FO images were obtained without additional adjustment in 170 of 200 simulated cases (85.0%) and in 28 of 30 intraoperative cases (93.3%). Simulated imaging showed excellent agreement with the actual osseous FO (Kappa = 0.96, $p < 0.001$; sensitivity = 0.99; specificity = 1.00), and intraoperative imaging demonstrated perfect agreement with the simulation (Kappa = 1.00, $p < 0.001$).

Conclusion: This technique provides reliable and accurate FO visualization, with excellent agreement between simulated, osseous, and intraoperative imaging. By simplifying the fluoroscopic process, this approach reduces the number of X-ray exposures required, thereby decreasing patient radiation exposure and shortening procedural time.

Keywords: foramen ovale, fluoroscopy, mobile C-arm X-ray system, trigeminal neuralgia, balloon compression

---

Introduction

Accurate puncture of the foramen ovale (FO) is essential for several percutaneous neurosurgical procedures in trigeminal neuralgia treatment, including percutaneous balloon compression (PBC), radiofrequency thermocoagulation, and glycerol injection.[1] The foramen ovale (FO) is situated in the lateral region of the middle cranial fossa at the posterior portion of the greater wing of the sphenoid. Medially, it is bordered by the foramen rotundum, and laterally, by the foramen spinosum. Because this bony canal is oriented nearly perpendicular to the skull base, the FO is not directly visible on standard frontal or lateral fluoroscopic views, making reliable fluoroscopic localization technically demanding and directly influencing procedural success and safety. Although the inferolateral trajectory introduced by Härtel remains the most widely adopted approach for FO puncture,[2] freehand puncture continues to pose considerable technical challenges, especially for less experienced surgeons. Misplacement of the needle can result in severe complications,

https://doi.org/10.2147/JPR.S557040
Received: 21 August 2025
Accepted: 8 January 2026
Published: 21 January 2026

including optic nerve injury, cavernous sinus penetration, internal carotid artery perforation, and jugular foramen involvement.[3]

To reduce these risks and improve accuracy, prior studies have explored using facial bony landmarks to guide the puncture trajectory.[4,5] However, these landmark-based techniques still suffer from variable reproducibility and often fail to provide a consistently clear FO view, particularly in patients with anatomical variations. Various imaging and image-guided modalities—such as fluoroscopy, CT, stereotactic frames, and neuronavigation—have been introduced to assist FO localization,[6–8] yet these systems either increase radiation exposure, prolong procedural time, or lack practical applicability in routine procedures. Among these, mobile C-arm fluoroscopy systems are the most widely used because of their convenience and lower radiation exposure. However, a standardized and reproducible protocol for achieving a clear FO view with C-arm fluoroscopy has not been established.[9–12] Traditionally, obtaining a clear fluoroscopic FO view requires first rotating the C-arm so that the X-ray beam passes between the maxilla and mandible toward the lateral skull base at a specific angle, followed by incremental tilt adjustments until the FO becomes visible. Although several studies have attempted to define optimal C-arm tilt angles, the reported ranges vary widely, and the absence of a unified reference plane has resulted in poor reproducibility across operators and patient populations. Some protocols further recommend aligning the C-arm along Härtel's trajectory before refining the orientation under fluoroscopic guidance. However, anatomical variability and operator experience often necessitate multiple adjustments, prolonging the procedure and increasing radiation exposure.

To overcome these limitations, we propose a novel C-arm fluoroscopic protocol that does not rely on fixed angular ranges in the sagittal plane. Instead, it uses visual alignment between selected anatomical landmarks and their fluoroscopic projections, enabling reproducible landmark visualization and improving both consistency and ease of application. We validated this method with both simulated fluoroscopy in three-dimensional (3D) virtual head models and actual intraoperative fluoroscopy during FO puncture procedures. Furthermore, we analysed the relevant anatomical angles to clarify the spatial principles underlying the technique.

Materials and Methods

Procedure of Our Method

This study involved both the methodological validation of the fluoroscopic imaging protocol and its clinical implementation. The research was reviewed and approved by the Medical Ethics Committee of the Second Affiliated Hospital of Zhengzhou University (Approval No.: JS2023028; Approval Date: January 7, 2023). Written informed consent was obtained from all participants for the use of their clinical and imaging data. Written informed consent for the publication of all clinical images included in this manuscript was also obtained from the patients. In addition, the patient shown in Figure 1 provided written informed consent for the publication of the image. All study procedures were conducted in accordance with the principles of the Declaration of Helsinki.

The patient was placed in a supine position, and a U-shaped metallic clip clipped at the root of the columella nasi, with its lowest point aligned to the subnasale, designated as Point A. Points B and C, representing the intersections of the lateral orbital margins and the superior extensions of the zygomatic arches bilaterally, were demarcated on the skin using surgical ink. The X-ray tube was initially positioned directly above the patient's face, and the first fluoroscopic image was acquired to confirm the full visualization of the orbital and facial bones. Subsequently, the C-arm was rotated around its transverse axis within the mid-sagittal plane of the body until Point A was either visually aligned with the imaginary line connecting Points B and C (Line A) or collinear with Point B (or C) and the central point of the X-ray tube in the lateral view. A second fluoroscopic exposure was then performed to verify whether Point A was approximately located at the midpoint of the imaginary line connecting the outermost points of the bilateral infraorbital margins (Line B). Following this, the X-ray tube was tilted along the C-arm toward the puncture side by 20° to 25° (radial angle) to obtain a clear image of the FO (Figure 1).

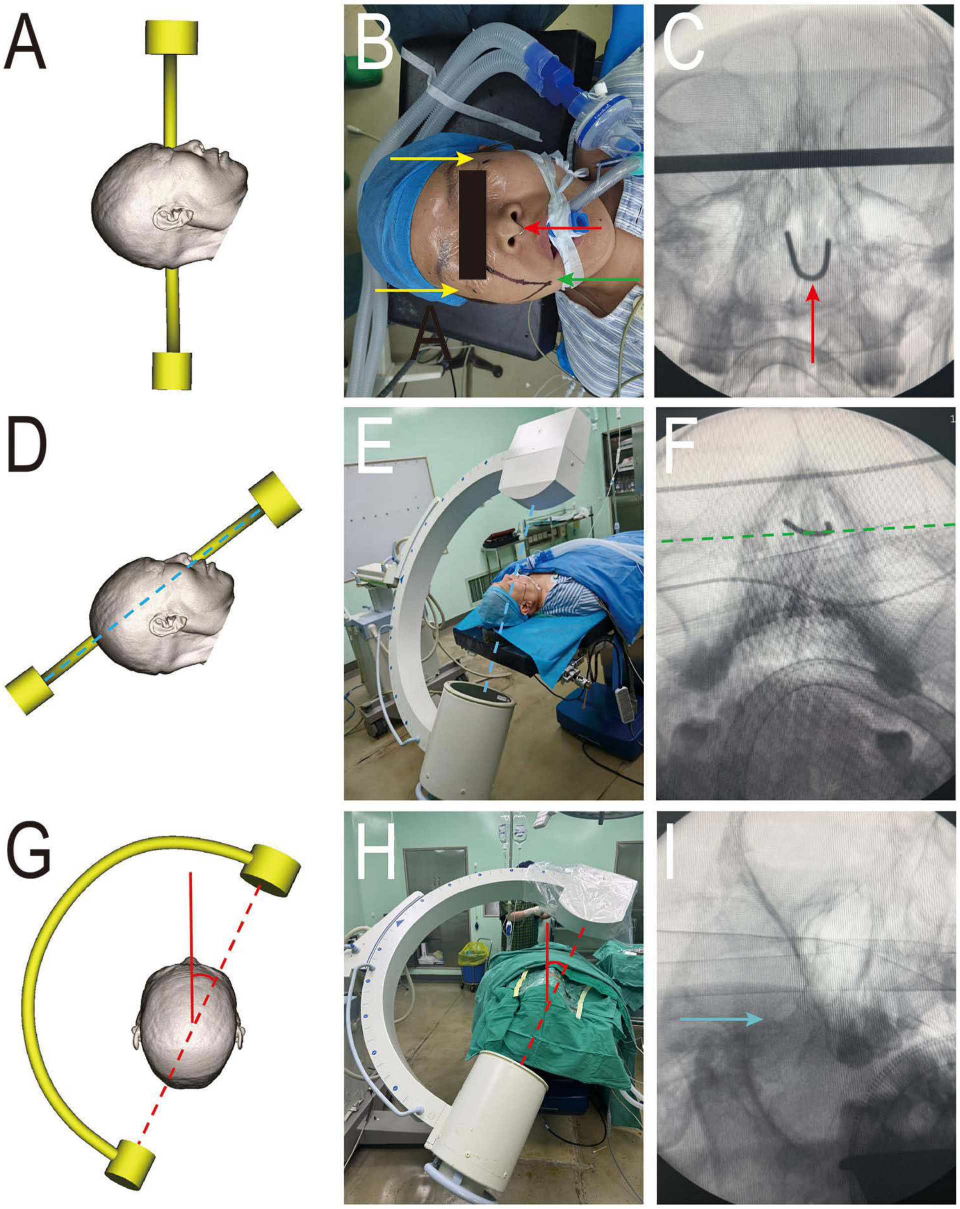

Figure 1 Process of FO fluoroscopy in actual operation. (**A**) The illustration shows the patient's position and the initial position of the C-arm. The X-ray tube is positioned directly to the patient's face. (**B**) Points A (the red arrow), B, and C (yellow arrows) are marked at the subnasale and the intersections of the lateral orbital borders and the superior extensions of the zygomatic arches on both sides, respectively. Point A is marked with the tip of a U-shaped metallic clip. The puncture point on the face is presented with a green arrow. (**C**) The first fluoroscopic imaging shows the orientation and range of X-ray projection. The position pointed to by the red arrow is the bottommost part (point A) of the metal U-shaped clamp. (**D** and **E**) The C-shaped arm is rotated toward the foot end until Point B (or Point C), Point A, and the centre of the X-ray tube are aligned collinearly (in the lateral view, as indicated by the blue dotted line. (**F**) The second fluoroscopic image verifies that Point A is approximately aligned with Line B between the bilateral outermost points of the suborbital margins (Line B, the green dotted line). (**G** and **H**) The red dashed line indicates the projected position of the X-ray beam. The C-shaped arm is tilted toward the puncture side by 25° (red angle) along the I–S axis. (**I**) The FO is presented under fluoroscopy with the blue arrow.

Verification of Our Method

The effectiveness of the proposed method was validated through two components. First, simulated fluoroscopy was performed on 3D-reconstructed head models derived from CT data to assess the feasibility and imaging characteristics of the FO using our method (Simulated Fluoroscopy Group). Second, the method was applied intraoperatively in patients undergoing FO puncture during PBC procedures to evaluate its clinical utility (Intraoperative Fluoroscopy Group).

Additionally, the operational characteristics of our method were further evaluated by comparing the number of X-ray exposures and procedural duration with those associated with FO determination using either conventional C-arm localization techniques and neuronavigation assistance. Finally, the anatomical foundations of our method were also investigated to clarify its rationale.

Simulated Fluoroscopy Verification

In the Simulated Fluoroscopy Group, head CT data (1 mm slice thickness, SOMATOM Definition Flash, SIEMENS, Germany) from 100 adult patients with intact craniofacial osseous anatomy were retrospectively collected between June 2020 and December 2024. The simulation was performed using 3D Slicer software (version 4.10.2). First, the raw images were transformed into a new linear coordinate system based on a reference plane defined by the bilateral optic nerve canals and perpendicular to the mid-sagittal plane. The software "Camera" was then used to simulate the X-ray tube of the C-arm and to establish a fluoroscopic viewing perspective. By adjusting parameters along the left–right (L–R) and inferior–superior (I–S) axes, controlled retroflexion or deflection of the virtual head was achieved, effectively simulating C-arm rotation and the resulting fluoroscopic visualization of facial structures.

Following the placement of Points A, B, and C on the surface of the virtual head according to our proposed protocol (Figure 2A), subsequent parameter adjustments in the "Volume Rendering" module enabled simulation of fluoroscopic visualization of the head. A simulated "blue clip" became clearly visible, with its inferior tip corresponding to Point A (the red point) (Figure 2B). The "camera" was then moved along the left–right (L–R) axis to induce backward extension of the virtual head until Points A, B, and C appeared approximately collinear in the visual field (Line A) (Figure 2C). After readjusting the parameters to restore the fluoroscopic effect, the image shows that Line A is nearly superimposed on Line B (the line connecting the outermost points of the bilateral infraorbital margins) (Figure 2D). Finally, a 20°–25° facial tilt was applied by moving the "camera" along the inferior–superior (I–S) axis, allowing evaluation of FO imaging characteristics under both bony reconstruction (Figure 2E) and simulated fluoroscopic conditions (Figure 2F). The complete virtual fluoroscopy workflow encompassing all steps shown in Figure 2 is demonstrated in Video 1.

Based on whether the FO was partially obscured by surrounding structures and required additional angular adjustments for optimal visualization, the FO fluoroscopic imaging was categorized into four distinct types (Figure 3). In Type I, the FO appears as an approximate ellipse or circle with less than one-third of its area obstructed. In Type II, more than one-third of the FO is obscured or shaped as a slit, necessitating minor angular adjustments along the "I–S" (IIa) or "R–L" (IIb)axis to enhance visualization. In Type III, the majority of the FO area is obscured, requiring adjustments across both axes. In Type IV, despite all possible camera adjustments, complete FO visualization cannot be achieved. For the simulated and intraoperative image assessments, both researchers were blinded to each other's evaluations and to the imaging group assignments (simulated vs intraoperative). All classifications were performed independently, and discrepancies were resolved by adopting the higher classification. The sensitivity and specificity of our method for acquiring a clear FO image in simulated fluoroscopy were evaluated using the 3D-reconstructed osseous FO, which was obtained through the same procedure in 3D Slicer and served as the gold standard.

Intraoperative Fluoroscopy Verification

The actual fluoroscopy procedure was performed in 30 patients with trigeminal neuralgia who underwent PBC at our department between February 2023 and January 2025. All patients received preoperative CT scans to ensure that the FO was sufficiently large to allow safe needle access. Fluoroscopic visualization of the FO was achieved using a mobile C-arm X-ray system (pulsed fluoroscopy mode; 69 kV, 7.5 mA; Siremobil Compact, Siemens, Germany). Once the FO was visualized, the puncture needle was inserted according to Härtel's orientation until its tip reached the skull base. Based on the fluoroscopic relationship between the needle tip and the FO, the needle was adjusted and advanced until it entered the FO. The FO imaging types observed intraoperatively were compared with the corresponding findings from preoperative simulation by an independent researcher.

To further assess the clinical efficacy of our proposed fluoroscopy-guided FO localization method (designated as group 1), additional comparative analyses were performed. Two retrospective control cohorts were included, comprising patients who underwent PBC by the same surgeons using alternative FO localization techniques between January 2018 and December 2022. The first control group (group 2) consisted of 12 patients who underwent conventional fluoroscopy-

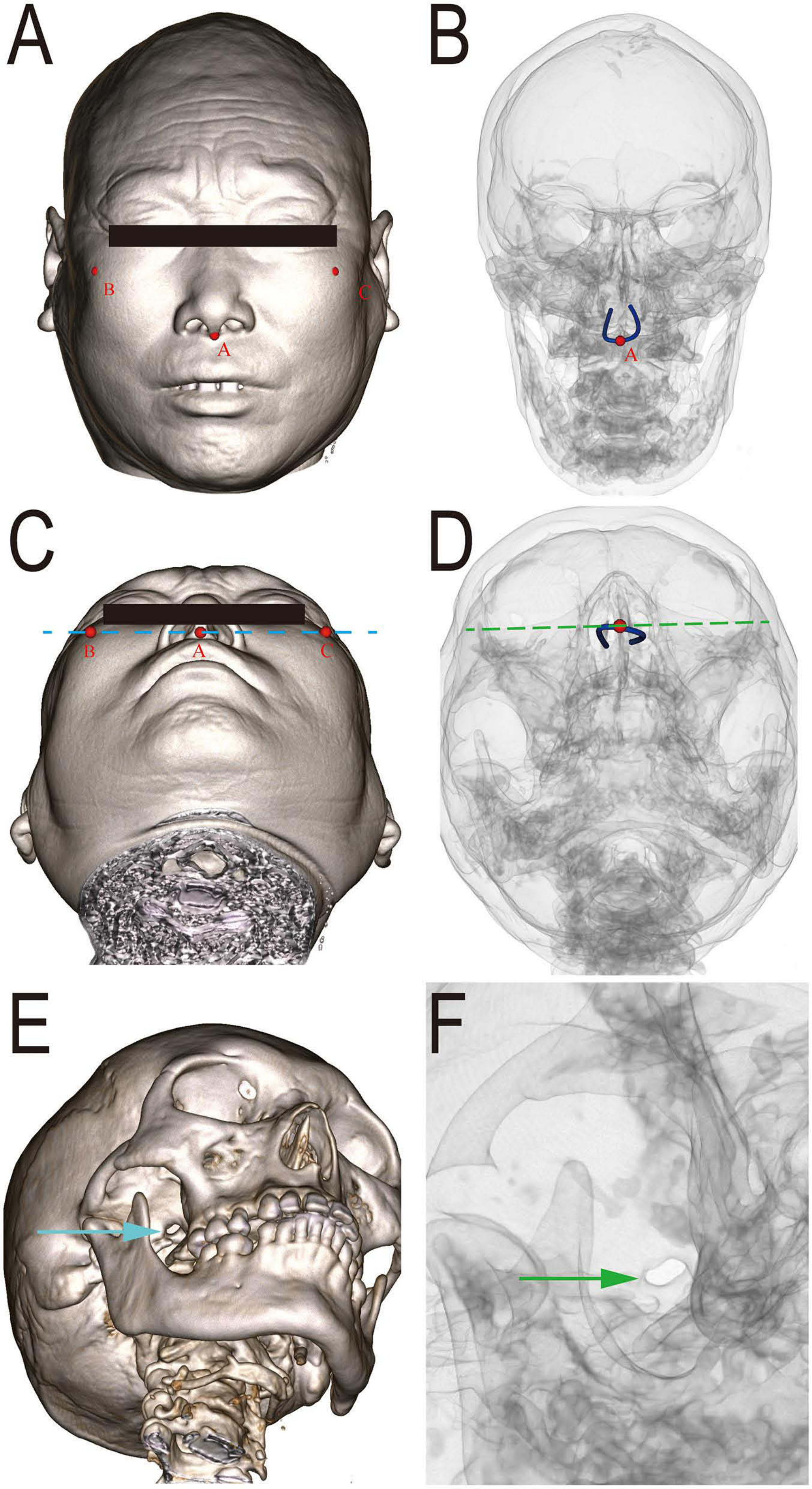

Figure 2 Workflow of simulated fluoroscopic verification. (**A**) Virtual head model with Points A, B, and C marked on the facial surface (red dots). (**B**) Simulated fluoroscopic rendering showing Point A (red dot), corresponding to the lowest point of the U-shaped metallic clip. (**C**) Adjustment of the virtual view along the L–R axis until Points A, B, and C (red dots) appear approximately collinear (Line A, blue dashed line). (**D**) Simulated fluoroscopic image showing Line A (green dashed line) nearly superimposed on Line B, which connects the bilateral infraorbital margins. (**E**) Application of a 20°–25° facial tilt to visualize the 3D-reconstructed FO (blue arrow). (**F**) Simulated fluoroscopic view demonstrating the FO (green arrow).

https://doi.org/10.2147/JPR.S557040

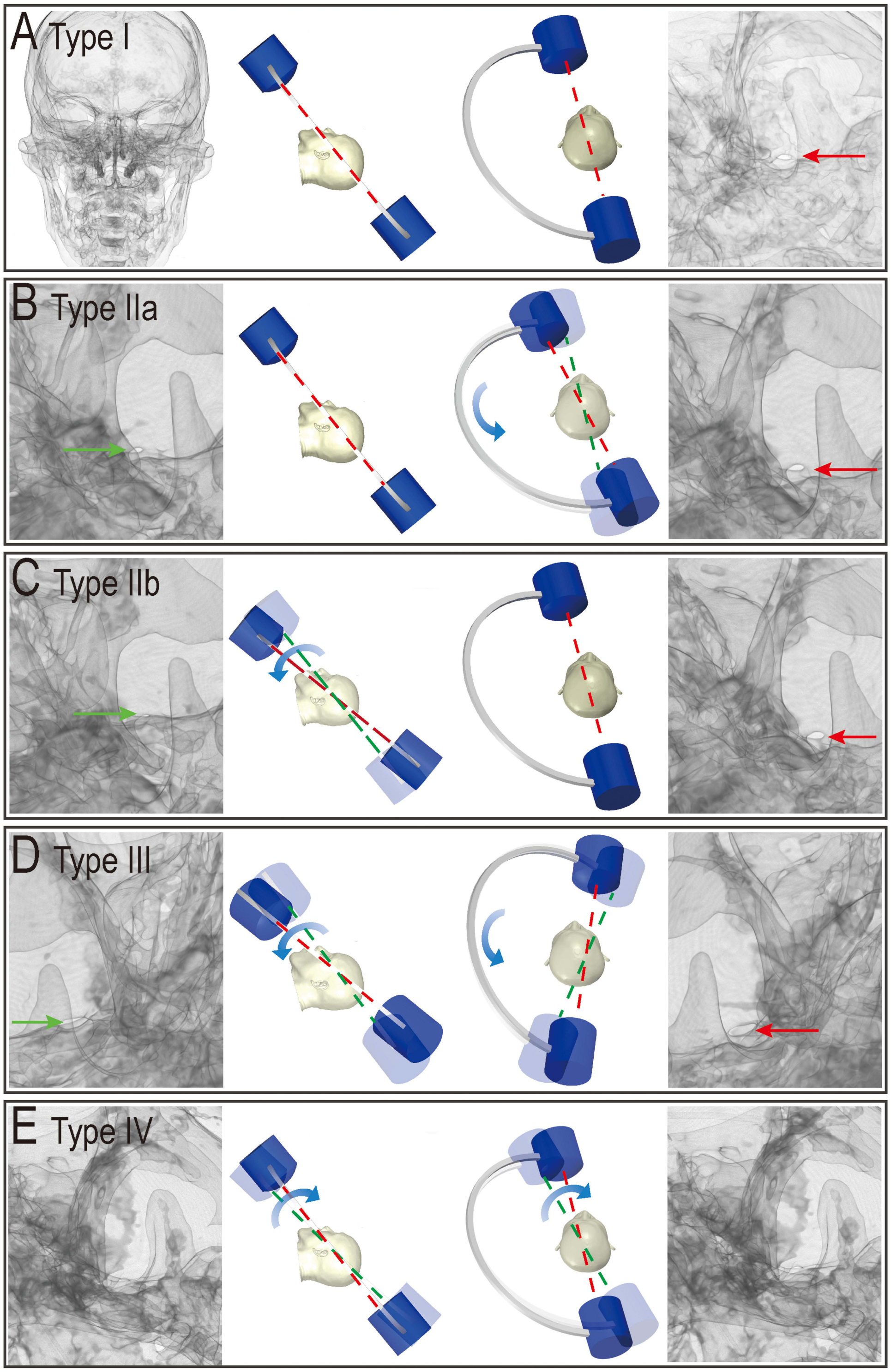

Figure 3 Different types (Type I–IV) of foramen ovale (FO) in simulated fluoroscopic imaging. The red dashed line and the green dashed line indicate the original and adjusted projection directions of the C-arm X-ray tube, respectively. The blue curved arrows indicate the direction of rotational adjustment of the C-arm. (**A**) Type I: The FO is fully visualized using the proposed method without requiring any additional angular adjustments (indicated by the red arrow). (**B**) Type IIa: The FO is partially obscured by the pterygoid processes of the sphenoid bone (green arrow). A slight additional tilt of the C-arm along I–S axis is sufficient to achieve a clear visualization of the FO (red arrow). (**C**). Type IIb: When the FO appears slit-like (green arrow), an additional rotation of the C-arm solely along the L–R axis yields an improved visualization of the FO (red arrow). (**D**) Type III: When the FO is slit-like and concurrently obscured by surrounding bony structures (green arrow), adjustments of the C-arm along both the I–S and L–R axes are required to obtain a clear FO view (red arrow). (**E**) Type IV: Optimal visualization of the FO cannot be achieved even with additional angular adjustments along both axes.

guided FO localization using a mobile C-arm system, with needle orientation determined by the intersection of the clivus and petrous ridge under fluoroscopic guidance. The number of X-ray exposures and the overall procedure duration were compared with those of group 1, using the same model of mobile C-arm system. The second control group (group 3) comprised 10 patients who underwent neuronavigation-guided FO localization (M7, Medtronic, USA) and was included for comparison of procedural time. Data collection and statistical analyses were conducted by an independent researcher.

Anatomical Principles Exploration

To elucidate the anatomical principles of the method, we selected 62 patients (31 males and 31 females, all aged over 50 years) from the 100 patients in virtual fluoroscopy for detailed geometric analysis on the randomly selected side. The measurements, processed by an independent researcher, included: (1) Angle A, defined as the rotational angle of the C-arm relative to the reference plane in the sagittal view; (2) Angle B, defined as the angle between the centerline of the FO canal and the reference plane in the sagittal view; (3) Angle C, where Line C is defined on a plane parallel to the reference plane and passing through the second molar root, connecting the midpoint between the maxilla and the mandibular ramus to the center of the external FO opening, and the angle formed between Line C and the sagittal plane in the transverse view is recorded as Angle C; (4) Angle D, defined as the angle between Line C and the reference plane in the sagittal view; and (5) Angle E, defined as the angle between Line A and Line B in the coronal view of the head (Figure 4). All measurements were obtained using Screen Protractor 4.0 software (Iconico, USA).

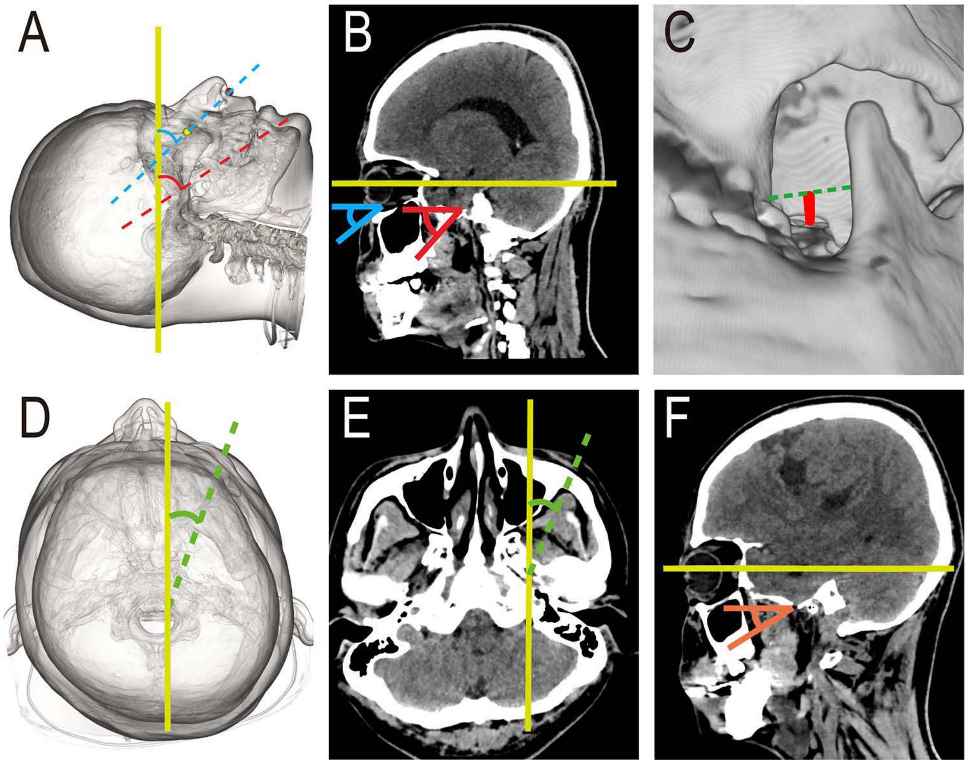

Figure 4 Anatomical angles measurement. (**A**) The yellow line represents the reference plane. The blue dashed line is collinear with Point A (red dot) and Point B (yellow dot), indicating the projection direction of the X-ray tube. The red dashed line represents the extended axis of the FO canal. The angles formed between the blue dashed line and the red dashed line with the reference plane (yellow line) correspond to Angle A (blue angle) and Angle B (red angle), respectively. (**B**) Angles A (blue angle) and B (red angle) are shown in the sagittal CT view with the yellow horizontal line representing the reference plane. (**C**) The green dashed line represents a line passing through the second molar root plane, parallel to the horizontal reference plane, extending between the lateral margin of the maxilla and the anterior margin of the mandibular ramus. Line C (red line) is defined as the line connecting the centre of the external opening of the FO to the midpoint of this green dashed line. (**D**) Angle C (green angle) is defined as the angle between Line C (green dashed line) and the sagittal plane (yellow line) in the transverse view. (**E**) Angle C (green angle) is shown in the transverse CT view and is defined as the angle between Line C (green dashed line) and the sagittal plane (yellow line). (**F**) Angle D (Orange angle) is defined as the angle formed between Line C and the reference plane (yellow line) in the lateral view.

Statistical Analyses

All statistical analyses were conducted using IBM SPSS Statistics version 26.0. Categorical variables are presented as frequencies and percentages (n, %). The Shapiro–Wilk test was used to assess the normality of continuous variables. Chi-square tests were used to examine the effects of patient characteristics (age, gender, and laterality) on procedural success and to evaluate the consistency between the fluoroscopic FO classification and the osseous FO classification derived from 3D reconstruction. The Mann–Whitney *U*-test was utilized to compare the number of X-ray exposures between groups, while the Kruskal–Wallis *H*-test was employed to compare procedure durations across multiple groups. For angle-related comparisons, the Mann–Whitney *U*-test was used to assess whether there were statistical differences in each angle between Type I imaging patients and non-Type I imaging patients. Differences between Angle A, Angle B, and Angle D were analyzed using a paired-samples *t*-test. The relationship between angle C and the tilt angle was assessed using Pearson correlation analysis. A p-value less than 0.05 was considered statistically significant.

Results

Fluoroscopic Image of FO

According to the most commonly used FO puncture approach, the optimal fluoroscopic FO should be consistently positioned between the maxilla's outer edge and the mandible's inner edge. It predominantly appeared as an oval-shaped transparent region, positioned superior to the ipsilateral petrous ridge with its long axis nearly parallel to this structure. Among the 200 sides from 100 patients in the Virtual Fluoroscopy Group, FO imaging without any additional adjustment was identified in 170 (85.0%) sides and categorized as Type I; 23 (11.5%) sides were classified as Type II; 4 (2.0%) sides as Type III; and 3 (1.5%) sides as Type IV (Table 1). No significant differences in gender (p = 0.579), age (p = 0.376), or side (p = 0.428) were observed among the imaging types (Table 1). For consistency analysis, the four imaging types were further merged into two categories: Type I (no adjustment required) and Types II–IV (requiring additional adjustment). Compared with the osseous FO visualized in the 3D reconstruction, the simulated fluoroscopic classification showed excellent agreement with it (Kappa = 0.96, p < 0.001; sensitivity = 0.99; specificity = 1.00), as shown in Table 2.

In the Intraoperative Fluoroscopy Group, the success rate for achieving Type I imaging was 93.3% (28/30). The remaining two cases (6.7%) required additional adjustments as Type II imaging (Table 3). Compared with the simulated

Table 1 Demographics and Classification of Foramen Ovale Imaging Types in the Virtual Groups

Groups	Type I	Type II	Type III	Type IV	P
Virtual fluoroscopy					
Gender					
Male	87 (83.7%)	12 (11.5%)	3 (2.9%)	2 (1.9%)	0.579
Female	83 (86.5%)	11 (11.5%)	1 (1.0%)	1 (1.0%)	
Age					
<50	54 (81.8%)	10 (15.2%)	2 (3.0%)	0 (0%)	0.376
>50	116 (86.6%)	13 (9.7%)	2 (1.5%)	3 (2.2%)	
Side					
Left	87 (87%)	10 (10%)	1 (1%)	2 (2%)	0.428
Right	83 (83%)	13 (13%)	3 (3%)	1 (1%)	
Total	170 (85%)	23 (11.5%)	4 (2%)	3 (1.5%)	

Notes: P values were calculated using Chi-square tests to assess the effect of sex, age, and side on the proportion of Type I cases. All P > 0.05, indicating no significant differences.

Table 2 Agreement Between Simulated Fluoroscopic Classification and Osseous FO Visualization

Imaging Method	3D Reconstruction		
		Type I	Type II–IV
Simulated X-ray	Type I	170 (85.0%)	0 (0.0%)
	Type II–IV	2 (1.0%)	28(14.0%)

Notes: Kappa = 0.96, p < 0.001; sensitivity = 0.99; specificity = 1.00.
Abbreviation: 3D, three-dimensional.

Table 3 Demographics and Classification of Foramen Ovale Imaging Types in the Intraoperative Fluoroscopy Groups

Groups	Type I	Type II	Type III	Type IV	P
Intraoperative Fluoroscopy					
Gender					
Male	12 (92.3%)	1 (7.7%)	0	0	0.201
Female	16 (94.1%)	1 (5.9%)	0	0	
Age					
>50	28 (93.3)	2 (6.7%)	0	0	
Side					
Left	10 (90.9%)	1 (9.1%)	0	0	0.685
Right	18 (94.7%)	1 (5.3%)	0	0	
Total	28 (93.3%)	2 (6.7%)	0	0	

Notes: P values were calculated using Chi-square tests to assess the effect of sex, age, and side on the proportion of Type I cases. All P > 0.05, indicating no significant differences.

FO imaging generated in 3D Slicer, the actual fluoroscopic classifications showed perfect agreement (Kappa = 1.00, $p < 0.001$), as shown in Table 4. Theoretically, our method can reliably achieve an FO image with three fluoroscopic interventions: first, confirming that the X-ray beam is perpendicular to the face and encompasses all relevant bony structures; second, ensuring collinearity between Point A and the line connecting the bilateral outermost points of the orbital lower margin; and third, observing the FO after tilting the C-arm toward the puncture side. Actually, the median number of fluoroscopic interventions required to obtain clear fluoroscopy-guided FO images using our method (group 1) was 3 (0.25), with a median puncture time of 37.5 (10.25) minutes. In contrast, conventional fluoroscopy-guided FO

Table 4 Cross-Tabulation of Imaging Classification results Obtained by Two Methods in the Intraoperative Fluoroscopy Group

Imaging Method	3D Reconstruction		
		Type I	Type II–IV
C-arm Fluoroscopy	Type I	28 (93.3%)	0 (0.0%)
	Type II–IV	0 (0%)	2 (6.7%)

Notes: Kappa = 1.00, p < 0.001.
Abbreviations: C-arm, C-arm X-ray system; 3D, three-dimensional.

Table 5 X-Ray Exposures and Procedure Duration Between Groups

	Group 1	Group 2	Group 3	P
X-ray exposures				
Median (IQR)	3 (0.25)	4 (1.75)	—	0.006[a]
Procedure duration				
Median (IQR)	37.5 (10.25)	69.5(26)	53(10.25)	<0.001[b]

Notes: [a]P: The Mann–Whitney *U*-test was used to compare X-ray exposures between Group 1 and Group 2, revealing a statistically significant difference (p = 0.006). [b]P: The Kruskal–Wallis *H*-test was used to compare procedure duration among the three groups, with a statistically significant difference observed (p < 0.001).

Table 6 Comparison of Relevant Anatomical Angles Between Type I Imaging Patients and Non-Type I Imaging Patients

Angles	Mean Value (°)	Type I	Type II-IV	u	z	p
Angle A	50.93(3.23)	50.44(3.64)	52.03(1.47)	164.5	–0.623	0.533
Angle B	65.45 (4.16)	65.42(4.05)	66.99(13.05)	137.5	–1.224	0.221
Angle C	20.37(4.30)	20.36(4.52)	20.39(8.90)	128.0	–1.435	0.151
Angle D	50.39(1.83)	51.04(1.93)	50.23(1.29)	114.5	–1.735	0.083
Angle E	1.83(0.88)	1.86(0.90)	1.66(0.91)	148.5	–0.979	0.328

Notes: Median (IQR) shown. Mann–Whitney U test indicated no significant differences among all angles (all p > 0.05).

localization using a mobile C-arm system (group 2) required 4 (1.75) fluoroscopic exposures and 69.5 (26.0) minutes for puncture, while neuronavigation-guided FO localization (group 3) required 53 (10.25) minutes (Table 5).

Anatomical Angle Measurements

The measured angles were as follows: Angle A = 50.93 (3.23)°, Angle B = 65.45 (4.16)°, Angle C = 20.37 (4.30)°, Angle D = 50.39 (1.83)°, and Angle E = 1.83 (0.88)°. Angle B was significantly greater than Angle A (95% CI 12.02–15.03°, $p < 0.001$), whereas Angle A and Angle D did not differ significantly (95% CI –0.02–1.28°, $p = 0.056$). The mean ratio of sin(A) to sin(B) was 0.87 ± 0.05, while the ratio of sin(A) to sin(D) was 1.01 ± 0.04. Additionally, the mean value of sin(E) was 0.03 ± 0.01. No significant differences were observed in any of the five measured angles (A–E) between patients with Type I imaging and those with non–Type I imaging among the 62 cases. Mann–Whitney *U*-testing showed that all p values exceeded 0.05, as detailed in Table 6. Type I imaging was observed in 55 cases. Of these, 41 cases had an inclination angle of 20°, while 14 cases had an inclination angle of 25°. Angle C was significantly positively correlated with the tilt angle ($r = 0.413$, $P = 0.002$, Pearson's correlation analysis). The mean Angle C was 20.46 ± 2.60° for cases with a 20° inclination and 23.24 ± 3.07° for those with a 25° inclination. Type II imaging was observed in five cases. Specifically, two cases required an increased rotational angle towards the foot end, while three required a decreased tilt angle towards one side. For the two cases requiring an increased rotational angle towards the foot end, the measured Angle B values were 66.99° and 72.46°. The measured Angle C values for the three cases requiring a decreased tilt angle towards one side were 12.17°, 13.34°, and 15.22°. Type III imaging was observed in one case, with Angle B and Angle C measured at 75.32° and 24.46°, respectively. Type IV imaging was observed in another case, with Angle B measured at 84.09°.

Discussion

Although Professor Härtel's method is widely regarded as the classical approach for FO puncture, accurately reproducing the technique remains difficult in routine clinical practice, particularly for less experienced surgeons. As a result, adjunctive imaging modalities such as X-ray fluoroscopy, CT, and neuronavigation are often required to improve puncture accuracy. Among these options, the mobile C-arm is most commonly used due to its low cost, accessibility, and high maneuverability. From a historical perspective, fluoroscopic techniques for FO visualization have primarily followed two major approaches: iterative adjustment of the C-arm rotation until the FO is clearly exposed, and the use of fluoroscopically visible anatomical landmarks to guide fine adjustments of the C-arm trajectory.

Limitations of Angle-Based Methods

Angle-based protocols have been proposed for decades, yet they remain inconsistent and difficult to reproduce. For example, Tator et al and Gerber recommended rotating the C-arm 45°–55° toward the foot end and then tilting the head 35°–50° toward the unaffected side when the orbitomeatal line is perpendicular to the bed.[9,13] In contrast, Wang et al suggested using the auditory–nasal line as the reference plane, rotating the head 60° contralaterally, and tilting the C-arm 12°–18° caudally.[14] Later, Shen et al reported that optimal FO visualization required a 7°–17° tilt toward the affected side and a 30°–50° caudal tilt of the C-arm.[15] The wide variation in recommended fluoroscopic projection angles across different studies cannot be attributed solely to differences in reference plane selection or procedural workflows; rather, a more fundamental explanation lies in the substantial anatomical variability of the foramen ovale itself. Cadaveric studies by Abdelghani et al[16] have demonstrated pronounced morphological and spatial differences of the foramen ovale between sides and across sexes. In this context, fluoroscopic protocols that rely on fixed projection angles inherently lack reproducibility in routine clinical practice.

Limitations of Landmark-Based Fluoroscopy

Landmark-based fluoroscopic approaches have received less systematic investigation and remain largely empirical. Although these methods typically begin with an approximate alignment following Härtel's trajectory and then refine the X-ray beam based on specific fluoroscopic features, many of the reported landmarks lack robust anatomical or geometric justification. Examples include the fluoroscopic intersection of the "arc-shaped line of the middle cranial fossa"[17] or the point at which the temporomandibular joint capsule occupies half of the mandibular neck width,[18] as well as the projection-based method described by Kim et al,[19] which identifies the FO by aligning the mandibular angle with the occipital cortical line but similarly lacks quantitative anatomical justification. Such features are highly operator-dependent and can vary substantially with craniofacial type, head rotation, fluoroscopic magnification, and mandibular positioning.

De Córdoba et al proposed a hybrid protocol combining a 25°–40° horizontal rotation with a 10°–25° tilt,[20] providing an intuitive and clinically practical approach. However, similar to other angle-based strategies, the recommended angle ranges remain relatively broad, and their applicability can be influenced by the patient's initial head position and the reference plane used during fluoroscopy. Moreover, because reproducible anatomical rules for determining these angles are still lacking, operators may need multiple adjustments to obtain an optimal FO view. Such variability is generally manageable in typical anatomy but may become more pronounced in patients with features such as pterygoid hypertrophy, mandibular deviation, or slit-like foramina.

Advantages of Our Geometry-Based Landmark Method

The core requirement for optimal FO fluoroscopy is the rapid and accurate determination of the X-ray beam direction. Although virtual fluoroscopic simulation has been applied previously to assist FO visualization,[21] standardized rules for determining projection angles have not been established. Anatomically, two planes must be precisely controlled: (1) the sagittal incidence angle to the skull base, ensuring visualization of the FO region, and (2) the horizontal inclination relative to the mid-sagittal plane, preventing facial bone overlap.

Unlike traditional angle-preset methods, our approach determines the first angle by observing the relative movement of facial landmarks between direct view and fluoroscopy. This technique relies on the geometric principle that the shadow of a stationary object changes predictably as the light source rotates in a plane, allowing the projection angle to be inferred directly from shadow morphology. Consequently, variations in head posture or reference plane do not confound the determination of the projection angle. Moreover, aligning point A with the B–C line is visually simpler and more intuitive than aligning the two imaginary planes described in Härtel's method. For practicality, we selected a 20°–25° tilt range, as each unit on the C-arm's curved rail corresponds to 5°.

Anatomical Validation and Implications

Our anatomical angle analysis showed that although Angle A (the C-arm incidence angle) and Angle B (the FO canal angle) differed significantly in the sagittal plane, the mean sinA/sinB ratio of 0.86 indicates that Angle A still covers most of the FO area under fluoroscopy. The foot-end rotation angle in our study (~51°) was slightly higher than previously reported, which likely reflects differences in reference planes and in the criteria used to define a "clear" FO image. In contrast to Peris-Celda et al, who described the classical "setting sun sign" in which the petrous ridge crosses the mid-portion of the FO,[11] we considered the FO to be clearly visualized only when the petrous ridge lay entirely below it, ensuring full exposure of the canal for puncture alignment.

The near-zero difference between the visually estimated alignment (Line A) and the fluoroscopic alignment (Line B) further supports the accuracy of our visual–geometric method in determining the optimal foot-end rotation. Because the second molar root is an important landmark for localizing the FO on X-ray,[22] we introduced an auxiliary "Line C", connecting the midpoint of the maxilla–mandible gap at the second molar level to the center of the ipsilateral FO. The angle between Line C and the sagittal plane (Angle C) corresponds to the optimal horizontal projection through the FO, and it closely matched our proposed tilt range. Thus, tilting the C-arm according to this angle ensures accurate FO visualization. In addition, Angle D did not significantly differ from Angle A, indicating that small variations in Angle A do not noticeably alter the FO's appearance under fluoroscopy. The variations in FO morphology, canal orientation, and surrounding bony structures described by Peris-Celda et al help explain why incomplete FO visualization may occur.[11] Our geometric findings correspond with these observations: abnormal values of Angle C were frequently associated with Type II–IV visualization patterns, requiring additional adjustments of the X-ray projection to obtain an optimal view.

Impact of Anatomical Variability on FO Visualization

Despite the overall success of our method, several FO images (Types II–IV) were not fully visualized and required additional adjustments to the X-ray projection angles. Two major anatomical factors accounted for these incomplete visualizations: an oval-shaped foramen ovale partially obscured by adjacent bony structures, and a slit-like foramen ovale that limited fluoroscopic visibility. Obstructions located anterior to the FO (toward the X-ray source) were typically caused by the mandibular ramus, mandibular body, or an enlarged pterygoid process (Figure 5A–C). In contrast, posterior obstructions were often due to osteogenic hyperplasia near the internal opening of the FO or by the petrous ridge close to the petrous apex (Figure 5D–F). This observation is consistent with the anatomical variability reported by Abdelghani et al,[16] who demonstrated significant inter-individual differences in the foramen ovale and its surrounding cranial base structures. Our fluoroscopic findings further suggest that such variability can translate into differences in FO visualization, necessitating individualized adjustment of projection angles in certain cases.

Angle C—defined as the angle between Line C and the sagittal plane—proved particularly sensitive to individual anatomical variation. When Angle C was <20°, the FO was frequently blocked by the pterygoid root, requiring a greater lateral tilt to clear the obstruction. Conversely, when Angle C exceeded 25°, the FO tended to be obscured by the mandibular ramus, necessitating a smaller tilt. Because Angle C is largely determined by the horizontal distance from the FO to the mid-sagittal plane (typically 20–24 mm),[23] deviations from this range, especially when combined with pterygoid hypertrophy, may lead to incomplete visualization even after multiple adjustments.

In some individuals, the FO canal is oriented nearly perpendicular to the skull base or requires unusually large foot-end rotation due to atypical craniofacial morphology. Using Frankfort-Mandibular Plane Angle (FMA)-based

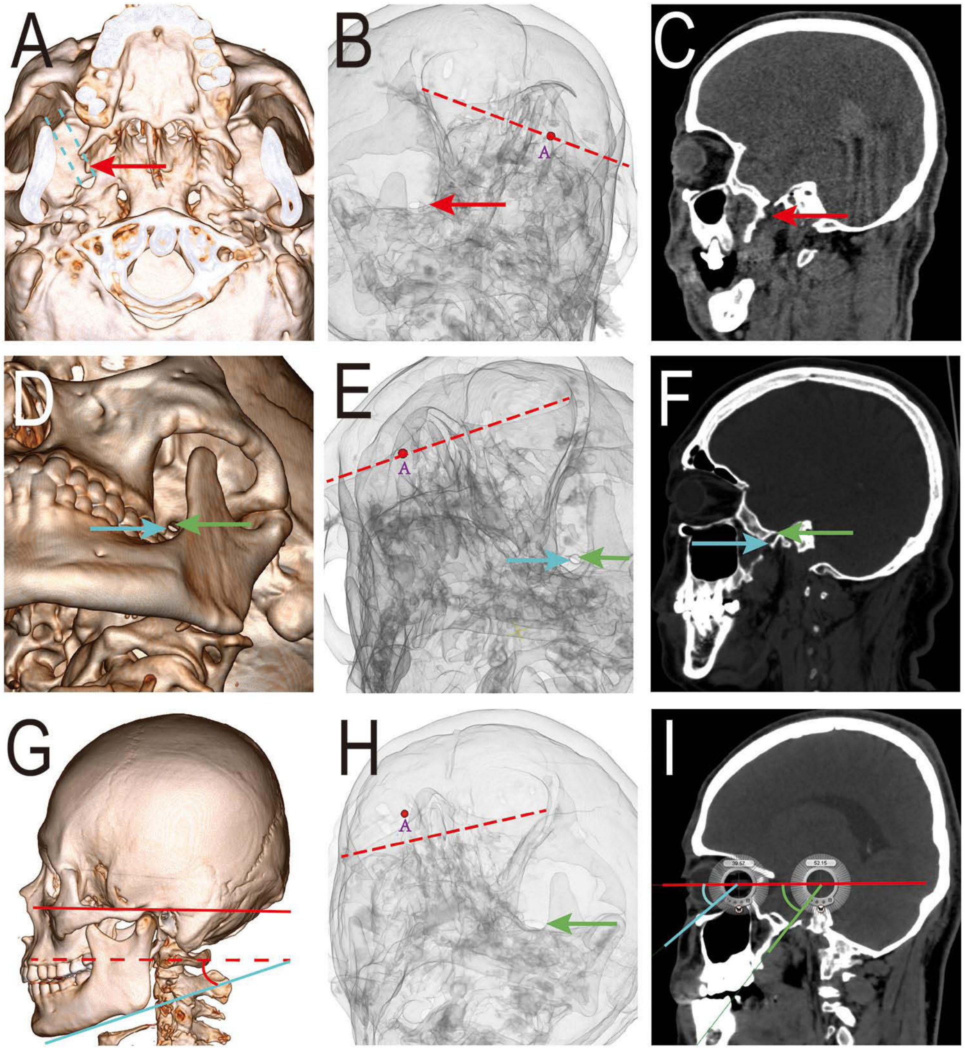

Figure 5 Influence of the large pterygoid process, osseous overgrowth at the inner opening of the FO canal, and low-skeletal facial type on FO fluoroscopy. (**A**) The red arrow indicates the large pterygoid process. The area between the two blue dashed lines represents the visualization of FO between the maxilla and the mandible in the 3D reconstructed skull. (**B** and **C**) The red dashed line indicates line B. The red dot represents Point A at the subnasale. The red arrow indicates the obstruction by the large pterygoid process. (**D**–**F**) The red dot represents Point A located at the subnasale. The blue arrow indicates the FO. The green arrow indicates the osseous overgrowth of the inner opening. The dashed line indicates Line B. (**G**) The low-skeletal facial type is depicted on the lateral view of a virtual head. The red solid line represents the orbitomeatal line. The red dashed line, parallel to the orbitomeatal line, and the blue line representing the mandibular plane form the FMA angle (red angle). (**H**) The red dot represents Point A located at the subnasale. Point A above line B (represented by the red dashed line), which means the increased rotation angle toward the foot end. The green arrow indicates the FO. (**I**) Showing the difference between angles A and B in this patient. The red line represents the reference plane, the blue line indicates the projection direction of the C-arm, and the green line represents the extended axis of the FO canal. The blue and green angles correspond to Angle A and Angle B, respectively.

skeletal classifications,[24,25] we observed that low-angle facial types required smaller rotation angles and often produced smaller projected FO images, necessitating further rotation toward the foot end (Figure 5G–I). In contrast, high-angle facial types required larger rotation angles, which increased the likelihood of the FO being obscured by the mandibular body or lateral pterygoid process, thereby requiring a reduction in rotation. Additionally, significant unilateral tooth loss may alter mandibular ramus positioning and disrupt FO imaging. This factor is clinically relevant because percutaneous balloon compression is frequently performed in older patients who may present with such dental changes.

Methodological Limitations and Practical Implications

The workflow in this study was initially developed within a virtual fluoroscopic environment in 3D Slicer, allowing analysis of the key geometric parameters required for FO visualization without additional radiation exposure. Subsequent intraoperative validation further demonstrated the feasibility of the workflow. Although this study did not directly measure patient radiation dose, comparison with the retrospective cohort undergoing conventional fluoroscopy-guided FO localization using a mobile C-arm system showed that our protocol required fewer fluoroscopic adjustments and a shorter puncture time; moreover, puncture time was also shorter than that observed in the neuronavigation-guided FO localization group.

The main limitation of this study is that the intraoperative validation included only 30 patients. The small sample size primarily reflects the limited number of trigeminal neuralgia cases eligible for percutaneous balloon compression. However, because this study focused on validating methodological feasibility and localization accuracy rather than assessing surgical outcomes, this sample size was adequate for methodological verification. Nevertheless, larger, multi-center, prospective studies are needed to further confirm the stability and generalizability of this workflow across different operators and clinical settings.

Conclusion

We developed a simple and reproducible mobile C-arm protocol that enables rapid determination of the optimal projection angle for FO imaging. This approach reduces unnecessary fluoroscopy adjustments, provides consistently clear FO visualization, and minimizes radiation exposure. The findings suggest that the protocol has meaningful practical value for FO imaging in clinical settings.

Acknowledgments

We sincerely thank all the patients who participated in this study for their trust and valuable support. We are also grateful to the Departments of Neurosurgery and Anesthesiology at the Second Affiliated Hospital of Zhengzhou University for their essential technical assistance and postoperative care throughout the research process. Special thanks go to the Department of Medical Imaging for their support in image processing and equipment coordination. All aspects of study design, data collection, analysis, interpretation, and conclusions were independently conducted and rigorously validated by the authors, who take full responsibility for the accuracy and integrity of the manuscript.

Author Contributions

Ting Qiu and Qiancheng Guo contributed equally to this work and share first authorship. All authors made a significant contribution to the work reported, whether that is in the conception, study design, execution, acquisition of data, analysis and interpretation, or in all these areas; took part in drafting, revising or critically reviewing the article; gave final approval of the version to be published; have agreed on the journal to which the article has been submitted; and agree to be accountable for all aspects of the work.

Disclosure

The authors report no conflict of interest concerning the materials or methods used in this study or the findings specified in this paper.

References

1. Liu H, Xu L, Zhao W. Puncture approaches and guidance techniques of radiofrequency thermocoagulation through foramen ovale for primary trigeminal neuralgia: systematic review and meta-analysis. *Front Surg*. 2023;9:1024619. doi:10.3389/fsurg.2022.1024619
2. Härtel F. Die behandlung der trigeminusneuralgie mit intrakraniellen alkoholeinspritzungen. *Dtsch Z Chir*. 1914;126(5):429–552. doi:10.1007/BF02800919
3. Kaur A, Singla R, Sharma R. An anatomical evaluation of normal and aberrant foramen ovale in skull base with its clinical significance. *Maedica*. 2022;17(2):357–362. doi:10.26574/maedica.2022.17.2.357
4. Kaur A, Singla R, Sharma R, Quites L, Fonseca Filho G. Percutaneous foramen ovale puncture: usefulness of intraoperative CT control, in the eventuality of a narrow foramen. *Stereotact Funct Neurosurg*. 2021;99(1):75–78. doi:10.1159/000509821
5. Prakash K, Saniya K, Honnegowda T, Ramkishore H, Nautiyal A. Morphometric and anatomic variations of foramen ovale in human skull and its clinical importance. *Asian J Neurosurg*. 2019;14(4):1134–1137. doi:10.4103/ajns.AJNS_243_19
6. Zhiping D, Chengwei W, Rui Y, Shengcheng W. Application of stereotactic surgical planning system in foramen ovale puncture for the treatment of trigeminal neuralgia. *Chin J Neurosurg*. 2015;31(10):1047–1050. doi:10.3760/cma.j.issn.1001-2346.2015.10.021

7. Guo W, Shi H, Wen X, Qian T. A simple method for foramen ovale puncture based on preoperative image simulation in percutaneous microcompression of the trigeminal ganglion. *Oper Neurosurg*. 2022;22(5):315. doi:10.1227/ons.0000000000000123
8. Zhigang G, Zhaohui L, Chao D, Xingli Z, Tian Y, Rui W. Application of stereotactic approach combined with 3D CT reconstruction in radiofrequency thermocoagulation of the trigeminal gasserian ganglion. *Chin J Neurosurg*. 2017;33(10):1030–1034. doi:10.3760/cma.j.issn.1001-2346.2017.10.015
9. Gerber AM. Improved visualization of the foramen ovale for percutaneous approaches to the gasserian ganglion. Technical note. *J Neurosurg*. 1994;80(1):156–159. doi:10.3171/jns.1994.80.1.0156
10. Grunert P, Glaser M, Kockro R, Boor S, Oertel J. An alternative projection for fluoroscopic-guided needle insertion in the foramen ovale: technical note. *Acta Neurochir*. 2010;152(10):1785–1792. doi:10.1007/s00701-010-0700-z
11. Peris-Celda M, Graziano F, Russo V, Mericle RA, Ulm AJ. Foramen ovale puncture, lesioning accuracy, and avoiding complications: microsurgical anatomy study with clinical implications: laboratory investigation. *J Neurosurg*. 2013;119(5):1176–1193. doi:10.3171/2013.1.JNS12743
12. Tatli M, Sindou M. Anatomoradiological landmarks for accuracy of radiofrequency thermorhizotomy in the treatment of trigeminal neuralgia. *Oper Neurosurg*. 2008;63(1):ONS129–ONS138. doi:10.1227/01.NEU.0000313569.43073.B2
13. Tator CH, Rowed DW. Fluoroscopy of foramen ovale as an aid to thermocoagulation of the gasserian ganglion: technical note. *J Neurosurg*. 1976;44(2):254–257. doi:10.3171/jns.1976.44.2.0254
14. Jun W, Yue H, Lianhai Y, Qinglai X, Baosen Z. Improved positioning skill in foramen ovale to treattri- geminal neuralgia by C-arm guidance. *J Pract Radio*. 2012;28(2):313–314. doi:10.3969/j.issn.1002-1671.2012.02.042
15. Zhenglin S, Liying C, Bin Z, Haibo L, Gaojie C. The value of C-arm localization and the puncture of foramen ovale under CT surface shaded display guidance. *J Pract Radio*. 2013;(6):1024–1025. doi:10.3969/j.issn.1002-1671.2013.06.039
16. Abdelghani N, Barut C, Ogut E. The investigation of cranial fossae in the intracranial cavity of fixed cadaveric skull bases: associations with sex, laterality, and clinical significance. *Surg Radiol Anat*. 2024;46(8):1305–1329. doi:10.1007/s00276-024-03408-8
17. Yuquan H, Shu H, Yunxia S, Xianghua Z, Haiyan C, Shenchu G. A new method for displaying the foramen ovale of the skull base under X-ray and its clinical value. *J Med Imag*. 2009;19(5):608–611. doi:10.3969/j.issn.1002-1671.2013.06.044
18. He L, Zhao W, PYP Su, et al. Novel fluoroscopic landmark to significantly facilitate the visualization of foramen ovale in treating idiopathic trigeminal neuralgia. *Reg Anesth Pain Med*. 2021;46(4):350–353. doi:10.1136/rapm-2020-102081
19. Lee SH. A novel method of locating foramen ovalefor percutaneous approaches to the TrigeminalGanglion. *Pain Physician*. 2019;22(4):E345–E350. doi:10.36076/ppj/2019.22.E345
20. De Córdoba JL, García Bach M, Isach N, Piles S. Percutaneous balloon compression for trigeminal neuralgia: imaging and technical aspects. *Reg Anesth Pain Med*. 2015;40(5):616–622. doi:10.1097/AAP.0000000000000292
21. Guo W, Wang Y, Du Y, Shi H, Shen S, Qian T. Enhancing visualization of the foramen ovale in percutaneous microcompression: a preoperative image simulation technique. *World Neurosurg*. 2024;189:312–316. doi:10.1016/j.wneu.2024.06.066
22. Zdilla MJ, Ritz BK, Nestor NS. Locating the foramen ovale by using molar and inter-eminence planes: a guide for percutaneous trigeminal neuralgia procedures. *J Neurosurg*. 2020;132(2):624–630. doi:10.3171/2018.11.JNS182276
23. Sthapak E, Pasricha N, Singh A, Bhatnagar R, Bedi RS. Foramen ovale and associated accessory foramina: a computerized tomography study to determine morphometry and analyze gender and age differences. *Natl J Clin Anat*. 2022;11(2):90–95. doi:10.4103/NJCA.NJCA_14_22
24. Johnson EL. The frankfort-mandibular plane angle and the facial pattern. *Am J Orthod*. 1950;36(7):516–533. doi:10.1016/0002-9416(50)90064-9
25. Schudy FF. The rotation of the mandible resulting from growth: its implications in orthodontic treatment. *Angle Orthod*. 1965;35:36–50.